*J. Fluid Mech.* (1988), *vol.* 186, *pp.* 199–222
*Printed in Great Britain*

# Simulation of particle dispersion in an axisymmetric jet

By J. N. CHUNG AND T. R. TROUTT
Department of Mechanical Engineering, Washington State University, Pullman,
WA 99164-2920, USA

(Received 5 September 1986 and in revised form 1 June 1987)

Particle dispersion in an axisymmetric jet is analysed numerically by following particle trajectories in a jet flow simulated by discrete vortex rings. Important global and local flow quantities reported in experimental measurements are successfully simulated by this method.

The particle dispersion results demonstrate that the extent of particle dispersion depends strongly on $\gamma_\tau$, the ratio of particle aerodynamic response time to the characteristic time of the jet flow. Particles with relatively small $\gamma_\tau$ values are dispersed at approximately the fluid dispersion rate. Particles with large $\gamma_\tau$ values are dispersed less than the fluid. Particles at intermediate values of $\gamma_\tau$ may be dispersed faster than the fluid and actually be flung outside the fluid mixing region of the jet. This result is in agreement with some previous experimental observations. As a consequence of this analysis, it is suggested that there exists a specific range of intermediate $\gamma_\tau$ at which optimal dispersion of particles in the turbulent mixing layer of a free jet may be achieved.

## 1. Introduction

Particle dispersion by turbulent shear flows is an intrinsic part of many important technological processes. Typical examples include the dispersion of liquid fuel droplets in gas combustors and the mixing of coal particles by the input jets of coal fired power plants. In many of these processes the dispersion of the particles is a controlling factor in the efficiency and the stability of the process.

The majority of previous predictive efforts involving particulate dispersion in turbulent shear flows have employed flow models involving only the time average properties of the turbulence or have treated the turbulent flow as a random field (Crowe 1982). However, recent developments in the understanding of both bounded and free turbulent shear flows have shown that quasi-orderly structures can control the dynamics of the flow. Reviews of these results have been written by Ho & Huerre (1984) and Cantwell (1981). For the case of free shear flows such as mixing layers and jets it has also been shown, as discussed by Ho & Huerre (1984) that external forcing techniques can be used to control the global development of these flows.

These developments in the understanding of turbulent shear flows have important implications concerning the modelling of particle dispersion in these flows. Recently, it was suggested by Crowe, Gore & Troutt (1985) that particle dispersion in free shear layers might be strongly dependent on the timescale of the large organized structures in the flow.

To explore the connection between the organized flow structures and the particle dispersion process (Crowe *et al.* 1985), previous experimental results from several particle dispersion experiments were evaluated by plotting the particle dispersion as a function of a timescale ratio defined from the particle aerodynamic response time and a timescale related to the large turbulent structures associated with each flow.

The aerodynamic response time of a particle is given by $\tau_A = \rho_p d_p^2/18\mu$ where $\rho_p$ is the particle density, $d_p$ is the particle diameter and $\mu$ is the fluid viscosity. This quantity represents the time required by a particle, released from rest in a uniform flow, to reach 63% of the flow velocity assuming Stokes drag law is applicable. It is simply a measure of the aerodynamic responsiveness of a particle. The characteristic timescale for the large vortex structures in the mixing layer of a free jet is rigorously defined by $\tau_F = \delta(x)/U(x)$ where $\delta(x)$ is the measure of the local thickness of the jet mixing layer which increases as the mixing layer grows and $U(x)$ is the characteristic velocity for the mixing layer. Without losing the physical meaning, a constant single parameter, $\tau_F = D/U_0$, is chosen in this analysis for engineering applications, where $D$ is the diameter of the pipe which issues the jet and $U_0$ is the centreline velocity of the jet at the pipe exit.

The ratio of the two times, $\gamma_\tau = \tau_A/\tau_F$, should characterize the effectiveness of the large-scale structures for moving particles laterally in the mixing region. For $\tau_A/\tau_F \gg 1$, the particles will not have sufficient time to respond to the large vortex structures and will move in nearly rectilinear path. In this case the flow spreading rate will be larger than the lateral dispersion rate of the particles. For $\tau_A/\tau_F \ll 1$, the particles have sufficient time to respond to the changing velocity field of large eddies and should disperse laterally with the spreading rate of the fluid mixing layer. On the other hand, for the condition $\tau_A/\tau_F \sim O(1)$ the large organized vortices may be able to temporarily capture the particles and fling them beyond the fluid momentum mixing region giving rise to a lateral particle dispersion rate greater than the spreading rate of the mixing layer.

Crowe *et al.* (1985) plotted previous experimental results which indicate that enhanced particle dispersion was apparent at intermediate values of the timescale ratio parameter. In addition average particle dispersion rates greater than the average turbulent momentum spreading rate were also indicated at these intermediate timescales. These results imply that the organized turbulent structures produced by free shear flows may have the ability to fling intermediate scale particles outside the turbulent flow region. Although this phenomena had been noted previously by experimentalists (cf. Yule 1980) no satisfactory explanation of the mechanism of this phenomena had been previously put forward.

To examine this physical concept in a more quantitative manner a simple inviscid analytical model, a distributed vortex solution (Stuart 1967), was used to simulate the shear-layer flow by Crowe *et al.* (1985). Particles were then released at various positions in the flow. A modified Stokes drag relation was used to determine the force on the particles. The results from this simple simulation were in good qualitative agreement with the experimental results, substantiating that particles in the intermediate timescale range could be dispersed most effectively by the shear flow. The numerical results also demonstrated that the intermediate scale particles could be dispersed beyond their initial fluid streamline indicating that particle dispersion rates greater than the flow spreading rate were also possible. Some initial efforts to model particle dispersion in plane mixing layers using spectral techniques have also been made by Gore *et al.* (1985). The results also support the physical model previously discussed.

Stuart's (1967) flow simulation model involves a non-developing and non-interacting vortex distribution. This model is therefore only a very crude approximation to a real mixing layer. A simulation model which more closely produces the vortex dynamics of a real mixing layer, however, can be obtained using a discrete vortex element approach. The interactions between these vortex elements is then used to model the developing flow. This approach, first used extensively by Chorin (1973) has been employed with considerable success to model free shear flows. One of the earlier applications of this model was carried out by Ashurst (1977) in a two-dimensional simulation of the dynamics of the plane mixing layer. Ashurst's results, obtained using several thousand vortex elements, were able to demonstrate the vortex clustering and pairing apparent in mixing-layer experiments. Ashurst's results also show very good agreement with moderate-Reynolds-number experiments for mean flow development and for turbulence energy and shear stress profiles.

To extend the previous efforts in simulating particle motion in free shear flows, a more realistic flow model is needed. Based on the previously noted work it was determined that the discrete vortex model would be an appropriate choice for this study. The geometry selected was that of an axisymmetric jet, since that flow is most commonly used for particle dispersion experiments. The most restrictive assumption in the employed model involves the two-dimensional axisymmetric constraint applied to the vortex elements. This assumption is reasonable for the first few diameters of the real jet flow. However downstream of the initial jet development three-dimensional distortions in the vortex rings become readily apparent in flow-visualization studies discussed by Ho & Huerre (1984). Modelling three-dimensional phenomena accurately is a complex numerical task which requires extensive computational resources. A discussion of the current status in three-dimensional vortex-element computational studies is given in a review by Leonard (1985). Although limited by the two-dimensionality assumption, the present efforts seem a reasonable next step in developing the numerical simulation of particle motion in free shear layers and can be considered at least a first-order approximation to an actual jet flow.

The flow model employed here follows closely a previous study by Acton (1980) which used the discrete vortex model to simulate the large eddies in an axisymmetric jet. Acton's time averaged results were found to be in reasonable qualitative agreement with previous experiments indicating that a considerable portion of the large vortex dynamics of jets can be modelled as axisymmetric. Details concerning the chosen flow model and the particle motion relations are presented in the following section.

## 2. Mathematical modelling

### 2.1. *Modelling of the jet flow*

As discussed previously, the discrete vortex model employed by Acton (1980) was adopted for the flow simulation. The axisymmetric jet is assumed to form starting from the exit of a circular pipe into a still environment. The numerical simulation starts with the moment that the flow first leaves the exit of the pipe and follows the development of the ensuing jet.

The basic assumptions used in the flow model are that the flow is inviscid and incompressible and constrained to be instantaneously axisymmetric. The inviscid assumption is reasonable for modelling the large vortex structure motions since

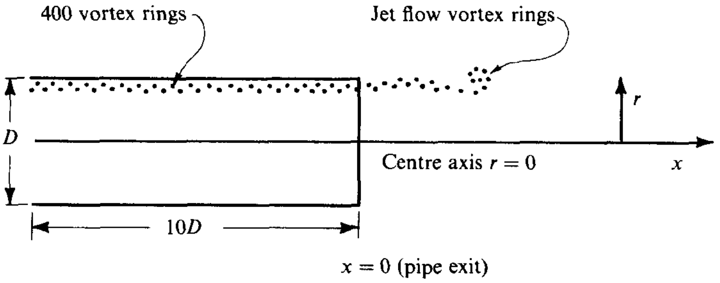

FIGURE 1. Schematic of flow simulation geometry.

numerous experiments in free shear flows have found the character of these structures to be relatively independent of Reynolds number. A discussion of the effect of Reynolds number on the development of free shear layers can be found in Ho & Huerre (1984).

Based on the previous assumptions the vorticity transport equation becomes simply

$$\frac{D\boldsymbol{\omega}}{Dt} = (\boldsymbol{\omega}\cdot\nabla)\boldsymbol{u}. \tag{1}$$

Where $\boldsymbol{\omega}$ and $\boldsymbol{u}$ are vorticity and velocity vectors respectively. Since the governing equation includes no viscous diffusion of vorticity the flow can be modelled by a superposition of discrete vortex elements. For the chosen geometry these elements are given the form of axisymmetric ring vortices. A schematic of the flow simulation geometry is shown in figure 1.

As each vortex element leaves the pipe exit it is replaced at the upstream end of the pipe tube by a new element, such that the number of vortex rings in the pipe remain constant during the calculation. After the vortex rings are released from the circular pipe, their movement is determined from the velocity induced by all the other vortices in the flow and their own self-induced velocity.

For a circular ring vortex of circulation strength $\Gamma$ with its core centre at $(x', r')$ as shown in figure 2, the Stokes stream function at $(x, r)$ is given by Lamb (1945) as

$$\Psi(x,r) = -\frac{\Gamma}{2\pi}(\sigma_1+\sigma_2)(K(\alpha)-E(\alpha)), \tag{2}$$

where

$$\sigma_1 = ((x-x')^2+(r-r')^2)^{\frac{1}{2}}, \tag{3}$$

$$\sigma_2 = ((x-x')^2+(r+r')^2)^{\frac{1}{2}}, \tag{4}$$

$$\alpha = \frac{\sigma_2-\sigma_1}{\sigma_2+\sigma_1}, \tag{5}$$

$$K(\alpha) = \int_0^1 ((1-t^2)(1-\alpha^2t^2))^{-\frac{1}{2}}\,dt$$

(complete elliptic integral of the first kind), (6a)

and

$$E(\alpha) = \int_0^1 (1-t^2)^{-\frac{1}{2}}(1-\alpha^2t^2)^{\frac{1}{2}}\,dt$$

(complete elliptic integral of the second kind). (6b)

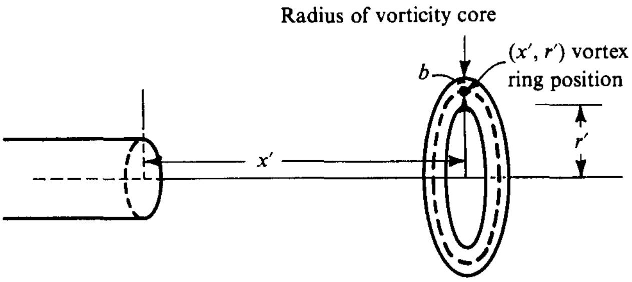

FIGURE 2. A typical vortex ring in flow simulation.

The induced downstream and radial velocity components are respectively

$$u(x,r) = -\frac{1}{r}\frac{\partial \Psi}{\partial r}, \quad v(x,r) = \frac{1}{r}\frac{\partial \Psi}{\partial x}. \tag{7}$$

Expanded, these relations give

$$u(x,r) = \frac{\Gamma}{2\pi r}\left\{\left[\frac{r-r'}{\sigma_1}+\frac{r+r'}{\sigma_2}\right](K(\alpha)-E(\alpha)) + \left(\frac{\partial K(\alpha)}{\partial \alpha}+\frac{\partial E(\alpha)}{\partial \alpha}\right)\left[\left(\frac{r+r'}{\sigma_2}-\frac{r-r'}{\sigma_1}\right)-(\sigma_2-\sigma_1)\frac{\dfrac{r-r'}{\sigma_1}+\dfrac{r+r'}{\sigma_2}}{\sigma_1+\sigma_2}\right]\right\}, \tag{8}$$

and

$$v(x,r) = -\frac{\Gamma}{2\pi r}\left\{\left(\frac{1}{\sigma_1}+\frac{1}{\sigma_2}\right)(x-x')(K(\alpha)-E(\alpha)) + \left(\frac{\partial K(\alpha)}{\partial \alpha}-\frac{\partial E(\alpha)}{\partial \alpha}\right) \times\left[\left(\frac{1}{\sigma_2}-\frac{1}{\sigma_1}\right)(x-x') - \frac{(\sigma_2-\sigma_1)\left(\dfrac{1}{\sigma_1}+\dfrac{1}{\sigma_2}\right)(x-x')}{\sigma_1+\sigma_2}\right]\right\}. \tag{9}$$

A curved vortex filament with a non-zero cross-sectional area has a finite self-induced velocity. This self-induced velocity, which is parallel to the axis of the ring vortex or more specifically the binormal direction, is given by Lamb (1945) based on the Kelvin formula for the velocity of a circular vortex ring of small cross-section in a perfect fluid, as

$$u_s = \frac{\Gamma}{4\pi r'}\left(\ln\frac{8r'}{b}-\tfrac{1}{4}+O\left(\frac{b}{r'}\right)\right), \tag{10}$$

where $b$ is the radius of the cross-section of the vorticity core. The value of the ratio $b/r'$ is somewhat arbitrary in this formulation as long as it is small compared to unity. Since $b(r')^{\frac{1}{2}}$ is a constant for the case of constant circulation, a value of $b(r')^{\frac{1}{2}} = 0.001$ was suggested by Acton (1980). This value is small enough such that the error term, $O(b/r')$, can be assumed negligible if $r'$ is not near the centreline. In addition, it was shown by Acton (1980) that the resulting self-induced velocity of the ring remains relatively insensitive to the choice of this ratio over a relatively wide range of values.

The flow within the pipe was simulated using a double row of 400 ring vortices located with equal axial spacing in a pipe length of 10 pipe diameters. The axial spacing of the rings is $0.05d$ (where $d$ is the pipe diameter or the jet exit diameter) and the radial spacing between rows is $0.025d$. It is assumed that the number of vortices is large enough to simulate the infinitely long vortex tube of the pipe flow. The total number of ring elements in the pipe array is kept constant during the simulation with new elements introduced at the upstream starting point as vortex elements are released at the exit of the pipe.

Once an array element leaves the pipe, it becomes part of the jet flow. The movement of the vortex is then based on the total induced velocity at its location. This velocity is induced in part, by all the other vortices in the pipe and those in the jet flow. In addition to the induced convection velocity, a self-induced velocity of the vortex element upon itself also contributes to the motion of the element. In mathematical form, the induced axial convection velocity for the $i$th vortex at the $j$th timestep is given by

$$\begin{aligned} u_{c,ij} = \sum_{\substack{k=1\\ k\neq i}}^{N} \frac{\Gamma_k}{2\pi r_{ij}} \biggl\{ & \biggl[\frac{r_{ij}-r_{kj}}{\sigma_{1,ikj}}+\frac{r_{ij}+r_{kj}}{\sigma_{2,ikj}}\biggr](K(\alpha_{ikj})-E(\alpha_{ikj})) \\ & +\left(\frac{\partial K(\alpha)}{\partial \alpha}-\frac{\partial E(\alpha)}{\partial \alpha}\right)\bigg|_{ikj}\biggl[\frac{r_{ij}+r_{kj}}{\sigma_{2,ikj}}-\frac{r_{ij}-r_{kj}}{\sigma_{1,ikj}} \\ & -(\sigma_{2,ikj}-\sigma_{1,ikj})\left(\frac{r_{ij}-r_{kj}}{\sigma_{1,ikj}}+\frac{r_{ij}+r_{kj}}{\sigma_{2,ikj}}\right)\bigg/(\sigma_{1,ikj}+\sigma_{2,ikj}\biggr]\biggr\}. \end{aligned} \tag{11}$$

The induced radial convection velocity for the $i$th vortex at the $j$th timestep is given by

$$\begin{aligned} v_{c,ij} = \sum_{\substack{k=1\\ k\neq i}}^{N} \frac{-\Gamma_k}{2\pi r_{ij}} \biggl\{ & \biggl[(x_{ij}-x_{kj})\left(\frac{1}{\sigma_{1,ikj}}+\frac{1}{\sigma_{2,ikj}}\right)(K(\alpha_{ikj})-E(\alpha_{ikj})) \\ & +\left(\frac{\partial K(\alpha)}{\partial \alpha}-\frac{\partial E(\alpha)}{\partial \alpha}\right)\bigg|_{ikj}\biggl[(x_{ij}-x_{kj})\left(\frac{1}{\sigma_{2,ikj}}-\frac{1}{\sigma_{1,ikj}}\right) \\ & -(\sigma_{2,ikj}-\sigma_{1,ikj})\left(\frac{1}{\sigma_{1,ikj}}+\frac{1}{\sigma_{2,ikj}}\right)(x_{ij}-x_{kj})/(\sigma_{1,ikj}+\sigma_{2,ikj})\biggr]\biggr\}, \end{aligned} \tag{12}$$

where

$x_{ij}$ = axial coordinate of $i$th vortex at $j$th timestep,
$r_{ij}$ = radial coordinate of $i$th vortex at $j$th timestep,
$\sigma_{1,ikj} = ((x_{ij}-x_{kj})^2+(r_{ij}-r_{kj})^2)^{\frac{1}{2}}$,
$\sigma_{2,ikj} = ((x_{ij}-x_{kj})^2+(r_{ij}+r_{kj})^2)^{\frac{1}{2}}$,
$\alpha_{ikj} = \dfrac{(\sigma_{2,ikj}-\sigma_{1,ikj})}{(\sigma_{2,ikj}+\sigma_{1,ikj})}$,
$N$ = total number of vortices in the system,
$k$ = $K$th vortex ring in the system.

The self-induced velocity of $i$th vortex at $j$th timestep is given by

$$\begin{aligned} u_{s,ij} &= \frac{\Gamma_i}{4\pi r'_{ij}}\left[\ln\left(\frac{8r'^{\frac{3}{2}}_{ij}}{B}\right)-\tfrac{1}{4}+O\left(\frac{B}{r'^{\frac{3}{2}}}\right)\right], \\ B &= b(r')^{\frac{1}{2}}, \\ &= 0.001. \end{aligned} \tag{13}$$

The total velocity components for each vortex element are then,

$$u_{ij} = u_{c,ij}+u_{s,ij}, \tag{14}$$

and

$$v_{ij} = v_{c,ij}. \tag{15}$$

The new downstream and radial positions ($(j+1)$th timestep) of each vortex ring can now be obtained to second-order approximation by

$$x_{ij+1} = x_{ij} + \tfrac{1}{2}(3u_{ij} - u_{ij-1})\,\Delta t, \tag{16}$$

$$r_{ij+1} = r_{ij} + \tfrac{1}{2}(3u_{ij} - u_{ij-1})\,\Delta t, \tag{17}$$

where $\Delta t$ is the timestep size.

As discussed by Chorin (1973) the high induced velocity which occurs when two small vortices are close together tends to invalidate the discrete vortex model. To remove this problem Chorin (1973) suggested the introduction of a 'smoothing' core to the vortices. Within the smoothing core the induced velocity acting on another vortex is assumed to vary linearly with radial position from zero at the core centre to the convection velocity calculated from (11) and (12) at the edge of the smoothing core. This vortex with a smoothing core is called a 'vortex blob' by Chorin (1973). The smoothing core is equivalent to a small viscosity which allows the vorticity to diffuse. The effect of the smoothing core on the numerical simulation is not cumulative, and most importantly, the results are independent of the size of the core if it is relatively small. In this analysis, the smoothing core radius is defined as a constant fraction (one fifth) of the ring radius. This assumption follows the development by Acton (1980).

The system is non-dimensionalized based on the following characteristic scales. All velocities are scaled by $U_0$, the centreline velocity in the pipe. The dimensionless downstream and radial distances, $X$ and $R$, are scaled with $D$, the pipe diameter, and time is thus scaled with $\tau_F = D/U_0$.

Since the pipe flow is assumed to be a vortex tube, the strength per unit length of this vortex tube, $\kappa_0$, is equal to $U_0$. The strength of each vortex element in the pipe vortex array is therefore equal to,

$$\Gamma = \frac{\kappa_0 D}{n}, \tag{18}$$

where $n$ = number of vortex rings in a pipe length of one diameter. The pipe vortex rings are driven downstream at a constant convection velocity $U_p$. A value of $U_p$ equal to 0.5 $U_0$ was determined for this simulation.

### 2.2. *Modelling of the particle motion*

To predict the particle motion in the jet flow a Lagrangian approach is followed. The trajectory of each particle in the flow is predicted directly from the equation of motion. The basic assumptions in the particle motion analysis are:

(i) All particles are non-deformeable solid spheres.

(ii) The density of the particles, $\rho_p$, is assumed large compared to the density of the fluid, $\rho$.

(iii) Particle–particle interactions are neglected.

(iv) The effect of the particles on the flow is neglected.

(v) Virtual mass force, pressure gradient force and Basset force are all neglected. An order of magnitude study based upon the equation of motion given in Maxey & Riley (1983) reveals that virtual mass and pressure gradient are of the order of the density ratio, $(\rho/\rho_p)$, and Basset force is of the order of $(\rho/\rho_p)^{\frac{1}{2}}$ if the drag force is of the order of $\gamma_\tau^{-1}$. Since $(\rho/\rho_p)$ is assumed to be $6\times10^{-4}$ for a typical gas–solid particle flow system in this study, the neglect of those forces is justified. It should be noted that Basset force may become relatively important for $\gamma_\tau > O(10^2)$ as compared to the drag force which is the dominant force in this analysis.

(vi) Other force fields including gravity are not included in this analysis. In a separate numerical study which includes the gravity on the earth's surface, the results show that for a Froude number $U_0^2/gD$, of 25, which is estimated as a lower bound for an inviscid jet, the global radial dispersion of particles represented by $D_R(T, N)$ as defined in (26) differs approximately by less than 1% for $\gamma_\tau = 0.05$, 1.5% for $\gamma_\tau = 1$, 4% for $\gamma_\tau = 10$ and 15% for $\gamma_\tau = 100$. In this investigation, we are mainly interested in the relatively large radial dispersions of particles which correspond to small and intermediate $\gamma_\tau$, therefore gravity is neglected in all the calculations presented in this paper.

The equation of motion for a particle can thus be written as

$$\frac{\mathrm{d}V_p}{\mathrm{d}t} = \frac{f}{\tau_A}(V - V_p), \tag{19}$$

where $V_p$ is the instantaneous particle velocity, $V$ is the instantaneous velocity of the fluid, $f$ is the modifying factor for the Stokes drag and $\tau_A$ is the particle aerodynamic response time. The factor $f$ is well represented for particle Reynolds numbers less than 1000 by $f = 1 + 0.15\,Re_p^{\frac{2}{3}}$ (Clift, Grace & Weber 1978), where $Re_p = |V - V_p|\,d_p/\nu$ with $d_p$ being the particle diameter and $\nu$ the kinematic viscosity of the fluid.

It should be noted at this point that the fluid viscosity is included in the particle motion equation but not in the governing flow equation. The reason behind this approach is that as a result of the drastic difference in the lengthscale between the two cases, particle motion is generally in the low-Reynolds-number category where the viscosity is a dominant factor. While for the jet flow, as discussed previously the motions have been shown experimentally to be relatively independent of viscosity and dominated by large scale structures.

The equation of motion may be non-dimensionalized using the following relations.

$$V_p^* = \frac{V_p}{U_0}, \quad V^* = \frac{V}{U_0}, \tag{20}$$

and

$$T = \frac{t}{D/U_0} = \frac{t}{\tau_F}. \tag{21}$$

This gives

$$\frac{\mathrm{d}V_p^*}{\mathrm{d}T} = \frac{f}{\tau_A/\tau_F}(V^* - V_p^*). \tag{22}$$

In addition several non-dimensional relations between the particle parameters and the flow parameters can also be defined: $\gamma_d = d_p/D$, $\gamma_p = \rho_p/\rho$ and $\gamma_\tau = \tau_A/\tau_F$. These parameters can be used to relate the diameter ratio and the particle Reynolds number to the implied flow Reynolds number, $Re = U_0 D/\nu$. This gives

$$\gamma_d^2 = \frac{18\gamma_\tau}{Re\,\gamma_\rho}, \tag{23}$$

and

$$Re_p = |V^* - V_p^*|\,\gamma_d\,Re. \tag{24}$$

The flow Reynolds number, $Re$, is involved due to the drag interaction between the particle and the fluid even though $Re$ is not used directly in the flow simulation.

It is noted that even though we have the following dimensionless groups specified in the particle dynamics, i.e. $\gamma_\tau$, $\gamma_\rho$, $\gamma_d$, $Re_p$ and $Re$, in view of (23) and (24), we decide to choose $\gamma_\tau$, $\gamma_\rho$ and *Re* as the independent parameters to be specified for each case in our calculations with the other parameters $\gamma_d$ and $Re_p$, directly related to them.

The values of $\gamma_\tau$, $\gamma_\rho$ and *Re* were selected based on the interests of practical applications. First, the timescale ratio, $\gamma_\tau$, was varied between 0.05 and 100. In an air jet with solid particles of diameter between 10 and 500 μm, $\tau_A$ is in the range of $6\times10^{-4}$ to 1.5 s. Typically $\tau_F$ is around 0.001 to 0.25 s. $\gamma_\rho^{-1}$ in this analysis is fixed at $6\times10^{-4}$ which is a typical value for solid particle in an air flow. Since the flow numerical simulation is based on the assumption of large-Reynolds-number inviscid flow, the choice of Reynolds number should be consistent with the flow assumption. In this analysis, the Reynolds number is set at 200000 which also corresponds to most practical particle jet situations.

It should be noted that according to (23) for a given Reynolds number, each $\gamma_\tau$ corresponds to a specific $\gamma_d$ because there is only one value for $\gamma_\rho$ in our analysis. Therefore, the variation of $\gamma_\tau$ represents the variation of particle size governed by the following relation,

$$\gamma_\tau \sim \gamma_d^2. \qquad (25)$$

## 3. Results and discussion

### 3.1. *Jet flow*

The development of the starting free jet into a still environment is shown in figure 3. Each cross represents the location of a vortex ring core for the top half of the jet. Plots of the instantaneous vortex patterns at dimensionless times from $T = 6$ to $T = 17$ are displayed. The large vortex cluster at the right-hand side of the $T = 8$ plot is indicative of the initial mushroom-type vortex normally produced by starting jets.

Two smaller clusters of vortices produced by unstable waves on the jet column can also be observed in the $T = 8$ plot upstream of the large starting vortex. Smaller clusters are labelled sequentially according to the order of formation in the figure for the purpose of keeping track of their interactions. These smaller clusters are produced by the jet at relatively regular intervals and as they proceed downstream they interact and subsequently merge with their nearest neighbours. To keep track of the interactions the combined vortex custers resulting from previous mergings are also indicated in the longer time plots.

The resulting vortex clusters are found to contain both even and odd number of the original clusters. This observation is in agreement with experimental results discussed in review by Ho & Huerre (1984) which reports both even and odd types of merging interactions occurring for both forced and natural mixing layers.

The current discrete vortex patterns shown in figure 3 are also in good agreement with those reported in Acton (1980) in which only discrete vortex patterns between $T = 8$ and $T = 12$ were shown.

Instantaneous downstream velocity traces computed at several radial positions from $x/D = 2$ are shown in figure 4. The first large-amplitude peak is produced by the arrival of the initial large-starting-vortex roll-up. Later large peaks can be associated with the arrival of one or more clusters of vortex elements. The vertical dash lines in $R = 0.4$ graph represent the instant that the centre of a vortex structure has just passed the $X = 2$ downstream location. The exact correspondence of the velocity peak and the arrival of the centre of a vortex structure at $R = 0.4$ was first noticed by Acton (1980). The number of peaks is not conserved between different radial

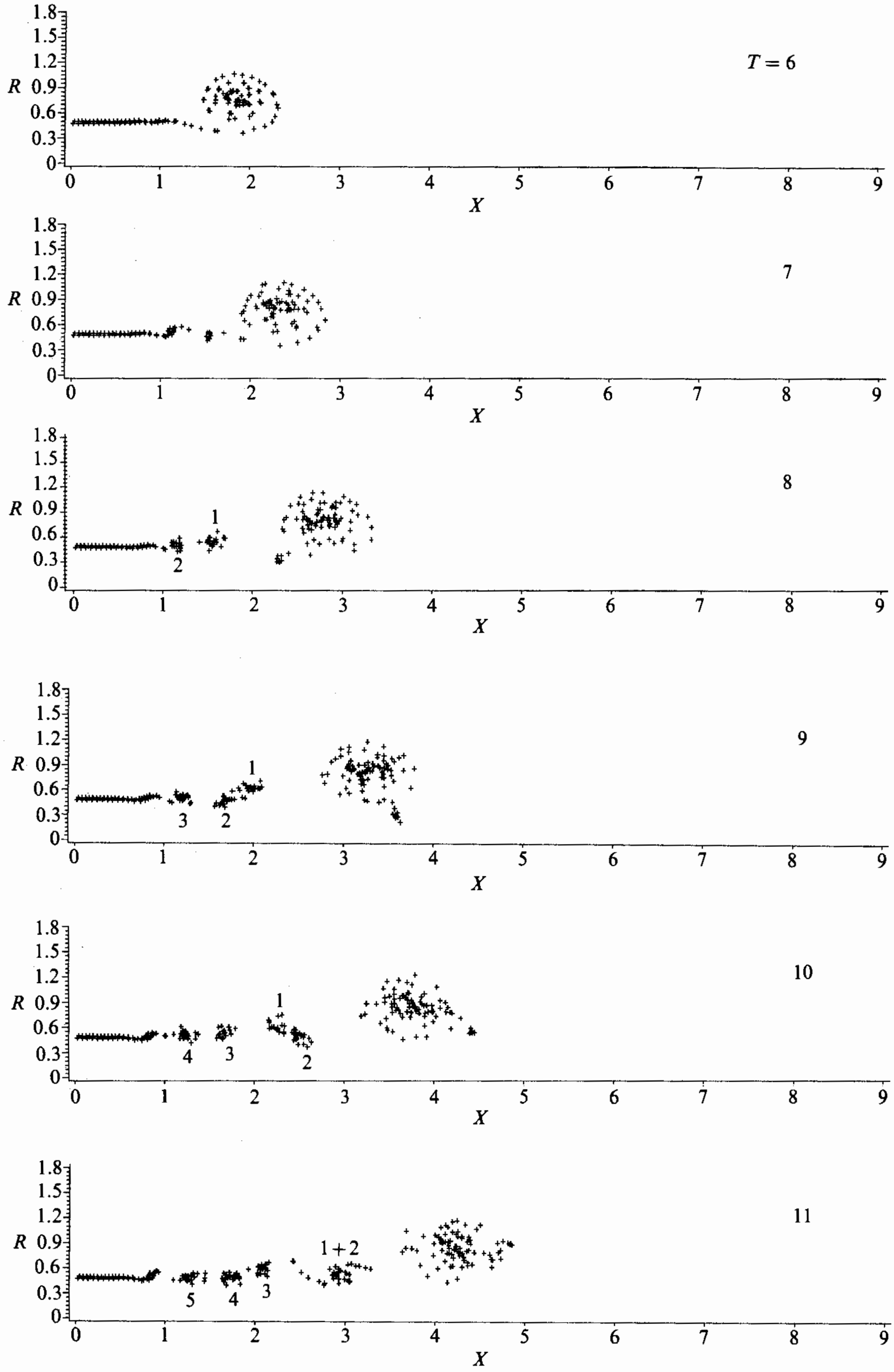

FIGURE 3. For caption see facing page.

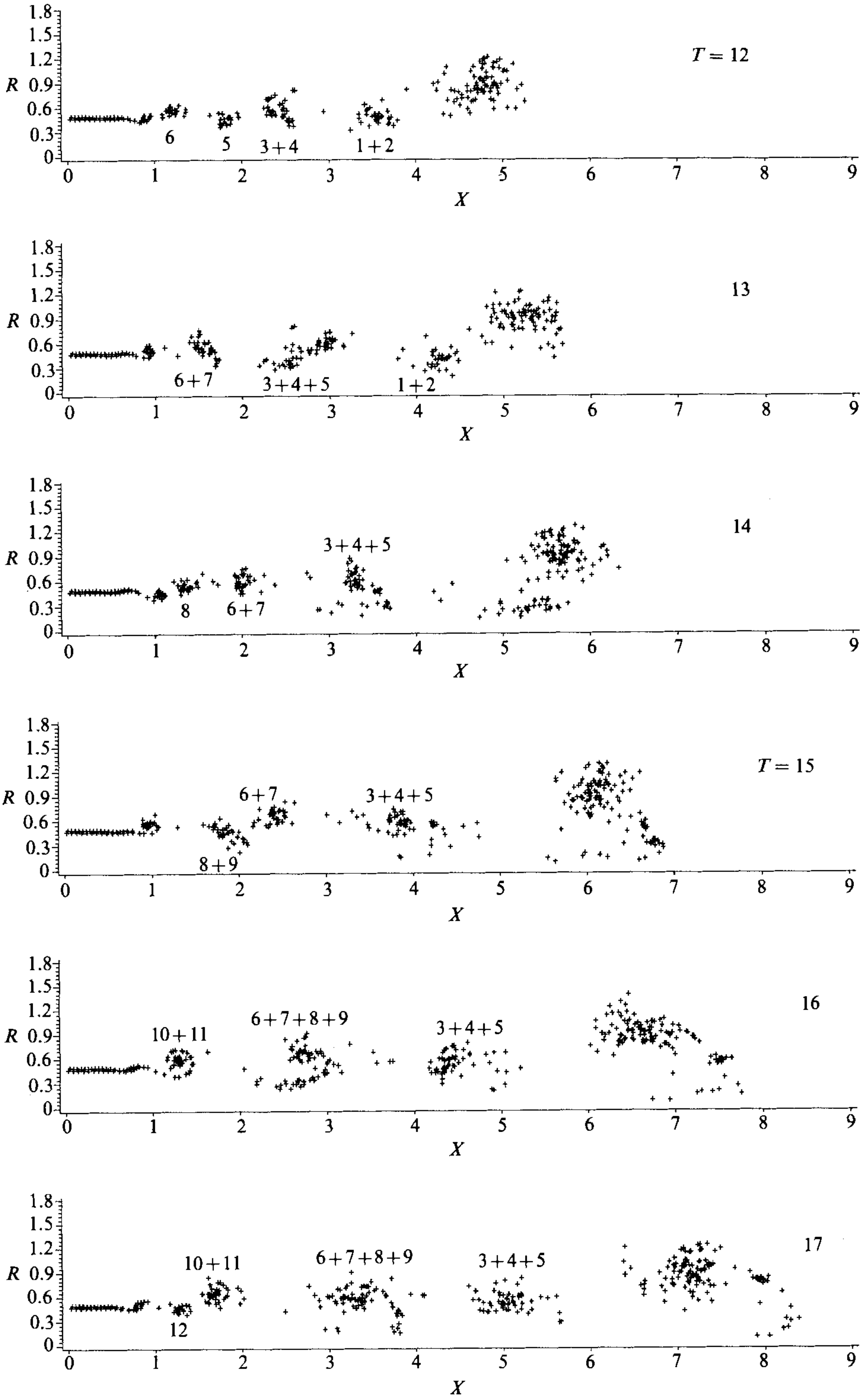

FIGURE 3. Jet flow development represented by discrete vortex elements between $T = 6$ and $T = 17$.

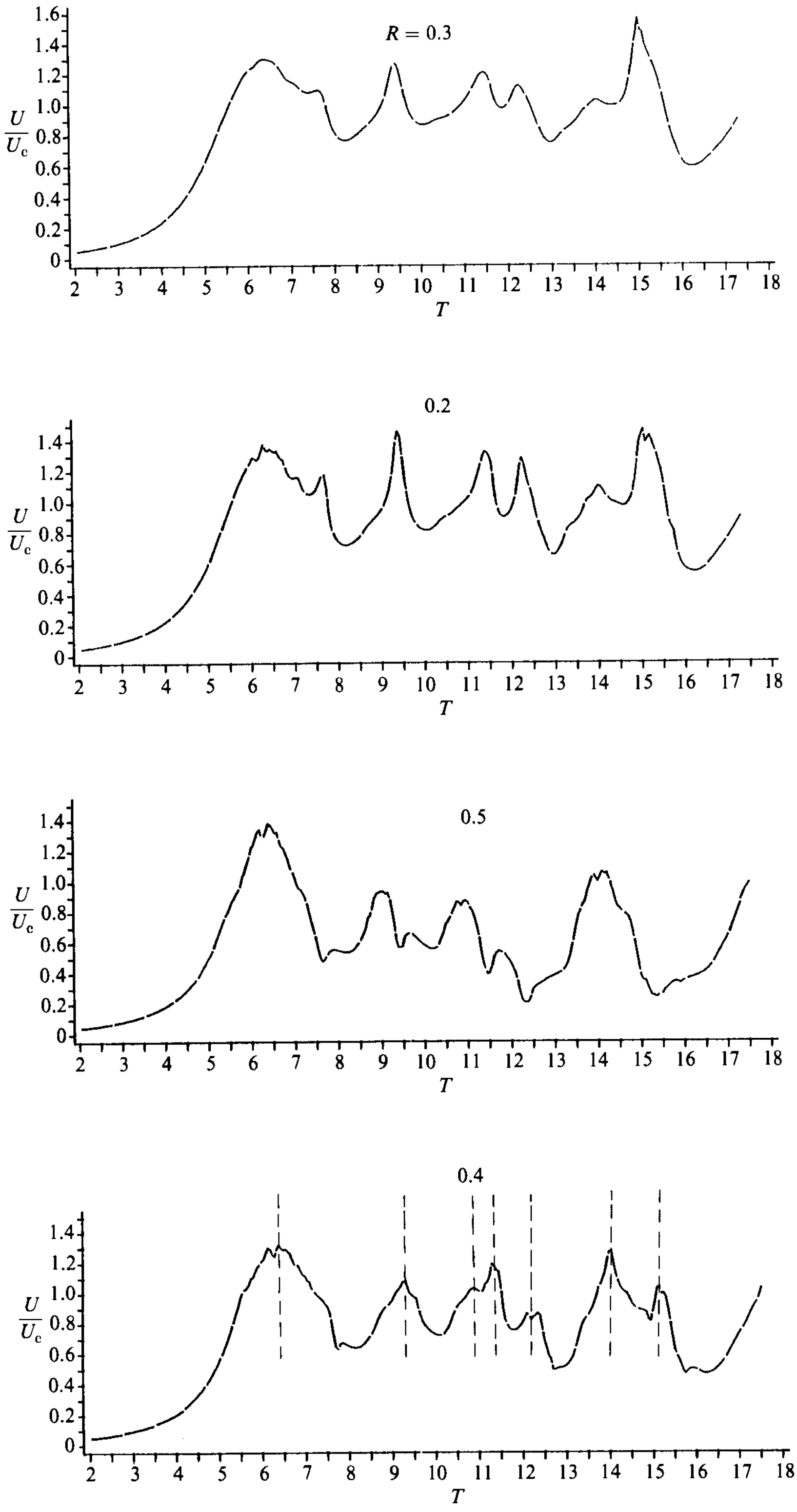

FIGURE 4. For caption see facing page.

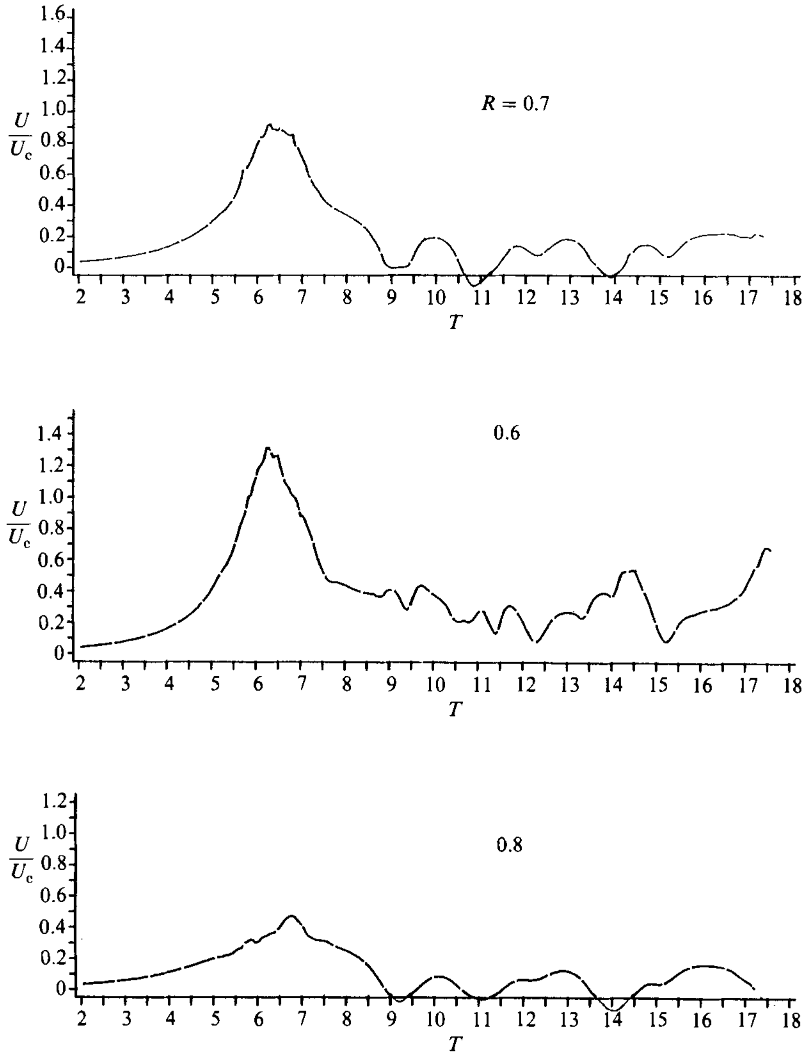

FIGURE 4. Instantaneous axial velocities at $X = 2$.

positions since the vortex cluster interactions displace the clusters in the radial direction, and therefore indications of the passage of each cluster may not substantially influence the instantaneous downstream velocity level at a particular radial position. This peak drop-out feature was noted by Acton (1980) and also occurs in laboratory experiments of free jets and mixing layers (Lau & Fisher 1975; Browand & Ho 1983). In the plane mixing-layer experiments by Browand & Ho (1983), it was shown that the fluctuating variation of the axial velocities as a function of time at a fixed downstream location exhibits a consistent trend. As the radial location is moved from the top edge of the mixing layer (low-speed side in Browand & Ho's experiment) towards the bottom edge (high-speed side), both the magnitude and the frequency of the signals increase and the spikes get narrower and more frequent. This same trend is shared by the current numerical predictions. We have also compared the current predictions of the axial velocities with those predicted by Acton (1980). A direct quantitative comparison is not feasible because Acton (1980)

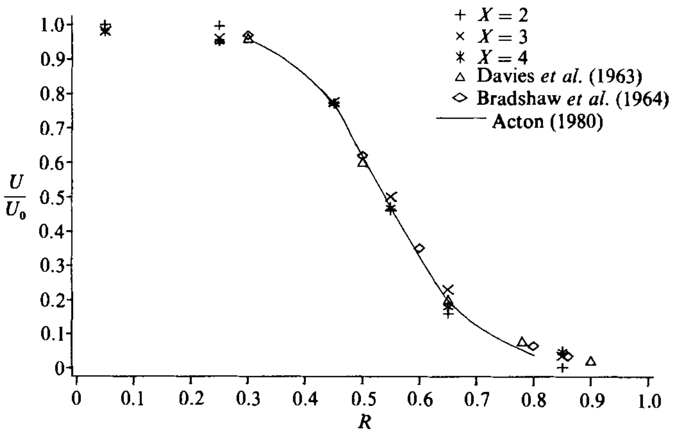

FIGURE 5. Normalized mean axial velocity profiles of the jet.

did not show the vertical scale in the plot. After a close comparison with the number of peaks, the location of peaks, and relative sizes of the fluctuations, we may conclude that the current results shown in figure 4 resemble closely those of Acton (1980).

Mean axial velocity profiles calculated from the numerical results for the downstream positions $x/D = 2$, 3 and 4 are shown in figure 5. The numerical results were averaged from initial times after the large starting vortex had moved a substantial distance downstream of the selected position. The present results show that the mean axial velocity profiles are approximately similar in the initial region of the jet development and agree well with previous experimental results of Davies, Fisher & Barratt (1963) and Bradshaw, Ferriss & Johnson (1964) and the numerical results of Acton (1980).

As seen in the above plots and comparisons, it may be concluded that the discrete vortex numerical simulation reasonably models the early development of the jet flow.

### 3.2. *Particle dispersion*

Particle dispersion by the jet flow is sampled in this study by introducing particles into the flow at the pipe exit ($x = 0$). For all the particle dispersion results presented in this paper, the particle initial velocity when it is introduced at the pipe exit is set to be equal to the local fluid velocity which is approximately uniform and is equal to $U_0$ at the pipe exit. The assumption that particles are in dynamic equilibrium with the flow is based on the experimental measurements of Yuu *et al.* (1978). In their experiments of a dust-laden round jet, they found that the particle velocities at the pipe exit were almost equal to the local fluid velocities for jet exit velocities ranging between 20 and 100 m/s and particle size of the order of 20 μm.

In figure 6(*a–d*) particle distribution patterns at $T = 17$ are shown for various $\gamma_r$ at a *Re* of 200000. Five streams of particles are introduced to the flow at radial locations, $R = r/D$ of 0.41, 0.43, 0.45, 0.47 and 0.49. One particle is released at each location during each timestep. This corresponds to a particle releasing rate of 1000 $U_0/D^2$ particles per radial distance per second. Particle injection starts at $T = 2$ and continues at a constant rate until $T = 17$. The reason for starting the particle injection at $T = 2$ instead of $T = 0$ is that we wanted to be sure that all the particles have plenty of opportunities to interact with the jet flow since particle–large scale structure interaction is the main subject of this study. The majority of the particles

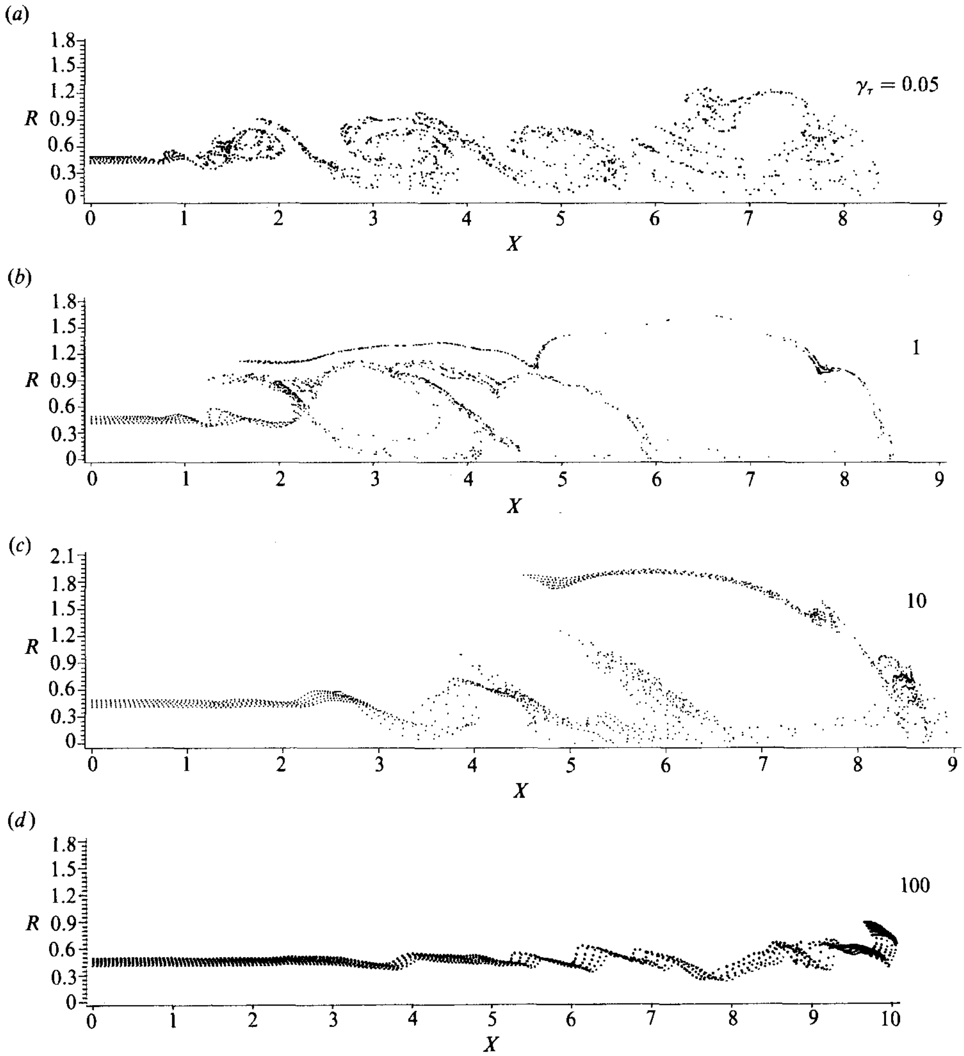

FIGURE 6. Particle distribution pattern at $T = 17$ for particles released between $R = 0.41$ and $R = 0.49$, (*a*) $\gamma_\tau = 0.05$; (*b*) $\gamma_\tau = 1$; (*c*) $\gamma_\tau = 10$; (*d*) $\gamma_\tau = 100$.

injected before $T = 2$ will penetrate through the leading vortex and enter the still environment. There are a total of 1500 particles in each plot of figure 6(*a–d*). As mentioned previously, each $\gamma_\tau$ corresponds to a specific $\gamma_d$ according to the relationship of $\gamma_\tau \sim \gamma_d^2$. For $\gamma_\tau$ of 0.05 as shown in figure 6(*a*), the particle size is small and its aerodynamic response time is much smaller than the flow characteristic time. In this case, the particles are closely following the flow streaklines as discussed earlier. It is clearly demonstrated in figure 6(*a*) that the particle distribution pattern gives a good visualization of the jet vortex structures in the jet flow and particle dispersion is approximately equal to that of the fluid.

As we increase the $\gamma_\tau$ to 1.0, the dispersion picture is quite different from that of $\gamma_\tau = 0.05$. As shown in figure 6(*b*), the particles may now be flung out of the large-vortex structures. In general, particles move away from the core of large-vortex structures. It should be noted that the outermost stream of particles in figure 6(*b*) is

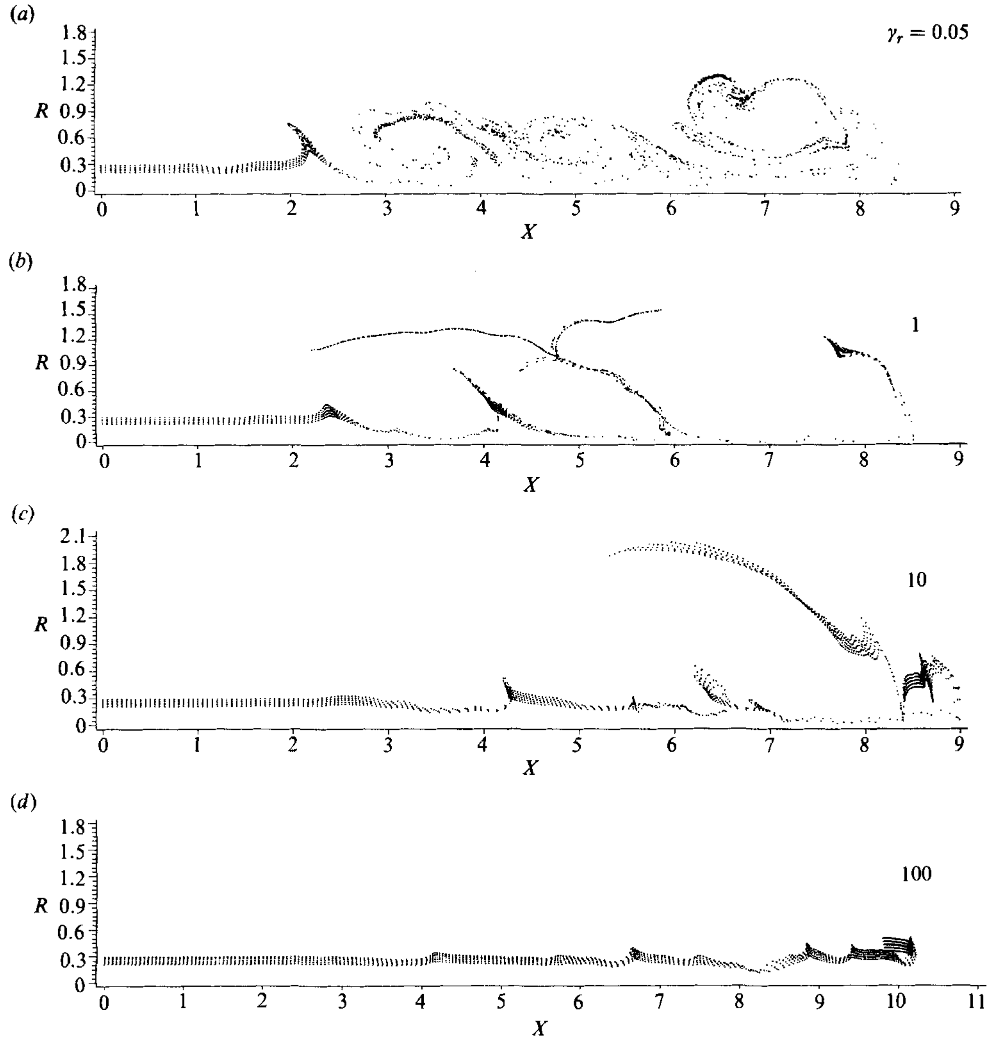

FIGURE 7. Particle distribution pattern at $T = 17$ for particles released between $R = 0.21$ and $R = 0.29$, (a) $\gamma_\tau = 0.05$; (b) $\gamma_\tau = 1$; (c) $\gamma_\tau = 10$; (d) $\gamma_\tau = 100$.

due to an accumulation of those particles which get flung out to the stagnant ambient region by the leading-vortex structure. These particles simply stay there because there is negligible fluid velocity outside the mixing layer. Therefore the radial dispersion of particles for $\gamma_\tau = 1.0$ is larger than that of $\gamma_\tau = 0.05$. This numerical simulation also verifies Yule's (1980) experimental observation that relatively larger droplets with their smaller drag/inertia ratios are seen to leave these eddies and penetrate the outer region.

For even higher $\gamma_\tau$, particles become less influenced by the flow structures as shown in figures 6(c) and 6(d) where at $\gamma_\tau = 10$, the radial dispersion is much reduced as compared with that of $\gamma_\tau = 1$ if we neglect the outer stream of particles flung up by the leading vortex. Only very limited dispersion is seen in figure 6(d) for $\gamma_\tau = 100$.

In practical applications, particles are usually present at all radial locations when they exit from the pipe. Therefore we also plotted the particle distribution patterns in figure 7 (a–d) with identical conditions to those in figure 6 (a–d) except the particles

| $R_{i0}$ | $\gamma_\tau$ | $D_R(17, 1500)$ | $\gamma_D(17, 1500)$ |
|---|---|---|---|
| 0.21–0.29 | 0.05 | 0.01266 | 1.059 |
| 0.21–0.29 | 1.0 | 0.01656 | 1.386 |
| 0.21–0.29 | 10 | 0.01506 | 1.260 |
| 0.21–0.29 | 100 | 0.00205 | 0.172 |
| 0.41–0.49 | 0.05 | 0.00717 | 1.032 |
| 0.41–0.49 | 1 | 0.01257 | 1.809 |
| 0.41–0.49 | 10 | 0.01618 | 2.328 |
| 0.41–0.49 | 100 | 0.00395 | 0.568 |

TABLE 1. Quantitative dispersion results for a starting jet

| $R_{i0}$ | $\gamma_\tau$ | $D_R(17, 1000)$ | $\gamma_D(17, 1000)$ |
|---|---|---|---|
| 0.21–0.29 | 0.005 | 0.01350 | 1.406 |
| 0.21–0.29 | 1 | 0.00865 | 0.901 |
| 0.21–0.29 | 10 | 0.00468 | 0.487 |
| 0.21–0.29 | 100 | 0.00113 | 0.118 |
| 0.41–0.49 | 0.05 | 0.00653 | 1.096 |
| 0.41–0.49 | 1 | 0.01120 | 1.879 |
| 0.41–0.49 | 10 | 0.00733 | 1.230 |
| 0.41–0.49 | 100 | 0.00209 | 0.351 |

TABLE 2. Quantitative dispersion results for an established jet

are introduced at $R = 0.21$, 0.23, 0.25, 0.27 and 0.29. For starting radial locations which are closer to the centreline, the particles will interact initially with the core flow of the jet which carries more momentum in the axial direction instead of the mixing-layer flow. This means that particles entering the jet at locations closer to the centreline will have higher axial momentum and therefore will in general experience less lateral displacement. In figure 7(*a–d*), we still observe the same general trends of particle dispersion at different $\gamma_\tau$ as those in figure 6(*a–d*) but generally with less radial displacement.

To quantify the results concerning the particle lateral dispersion, the radial global dispersion function at time $T$ is defined as the following,

$$D_R(T,N) = \left(\sum_{i=1}^{N} (R_i(T)-R_{i0})^2\right)^{\frac{1}{2}} / N, \tag{26}$$

where $N$ is the total number of particles in the system at time $T$, $R_i(T)$ is the dimensionless radial location of the particle $i$ at time $T$ and $R_{i0}$ is the radial location of particle $i$ at the jet exit.

To quantify the fluid dispersion of the jet flow, tagged fluid particles are introduced to the jet flow in a format identical to those of actual particles as described above. The global dispersion function for fluid particles is similarly defined and is given as $D_R^f(T,N)$. Then we define the ratio

$$\gamma_D(T,N) = \frac{D_R(T,N)}{D_R^f(T,N)}, \tag{27}$$

$\gamma_D(T,N)$ represents the ratio of particle dispersion to the fluid particle dispersion under identical conditions. $\gamma_D(T,N)$ may be considered to correspond reasonably

| $\gamma_\tau$ | $\gamma_D(17, 1000)$ | $Sc^{-1}$ (Yuu *et al.* 1978) |
|---|---|---|
| 0.05 | 1.406 | 1.32 |
| 1 | 0.901 | 0.89 |
| 10 | 0.487 | 0.54 |
| 100 | 0.118 | 0.11 |

TABLE 3. Comparison of current numerical predictions with experimental results of Yuu *et al.* (1978)

closely to the reciprocal of turbulent Schmidt number, $Sc = \epsilon_m/\epsilon_c$, where $\epsilon_m$ and $\epsilon_c$ are eddy diffusivity for momentum and mass diffusion respectively.

Tables 1 and 2 summarize the quantitative dispersion results based on the global particle dispersion function $D_R$ and the associated particle to fluid dispersion ratio, $\gamma_D$ for the free jet. In table 1, $N$ is equal to 1500 which includes all particles in the simulation at $T = 17$ (particles released between $T = 2$ and $T = 17$). In table 2, $N$ is equal to 1000 which includes only the particles released between $T = 7$ and $T = 17$. This table does not include the particles that are released between $T = 2$ and $T = 7$. It is observed that particles released between $T = 2$ and $T = 7$ are usually ingested by the leading large-vortex structure and therefore get dispersed dominantly by this leading large-vortex structure. In most of the industrial applications or experimental measurements, the jets have already reached a steady-state condition and the leading vortex structure is not present. Therefore results in table 1 are more representative of a starting jet while those of table 2 are thought to closely correspond to particle dispersion in an established jet. The particle release regions are specified in the tables, i.e. $R_{i0} = 0.21$–$0.29$ in the core region and $R_{i0} = 0.41$–$0.49$ near the edge of the jet.

It is seen that the results shown in tables 1 and 2 are consistent with our postulated physical concept that at some intermediate time ratios, particles may be dispersed beyond the fluid dispersion boundary. In the large-scale structure of a turbulent free jet, particle lateral dispersion seems to be most efficient for $\gamma_\tau$ being of the order of unity for particles exiting near the pipe wall because they interact primarily with the mixing layer structures. For particles released in the middle portion between the centreline and the pipe wall, only those particles with much smaller $\gamma_\tau$ are dispersed further than that of the fluid. This is because only particles with larger drag to momentum ratio (corresponding to smaller $\gamma_\tau$) are more likely to be captured by the large-scale vortex structures since the particles released in the middle portion between the centreline and the pipe wall usually encounter the lower outer edge of the mixing layer where the entrainment power of the fluid is weaker. It is plausible to assume that large-scale vortex structures in turbulent mixing layers are capable of dispersing particles of some intermediate $\gamma_\tau$ beyond the boundary of fluid dispersion. The experimental results of Yuu *et al.* (1978) on the turbulent Schmidt number are compared with our predictions in table 3. The result of Yuu *et al.* (1978) is the only experimental work found in the literature that is comparable to our numerical model, even though some differences still exist such as those listed as simplifying assumptions in the numerical model.

In table 3 a comparison is made between the experimental results of Yuu *et al.* (1978) and present calculations of $\gamma_D(17, 1000)$ for particles released at $r/D = 0.21$–$0.29$. The reason for comparing only with particles introduced in the middle region between centreline and the pipe wall is explained as follows. In the

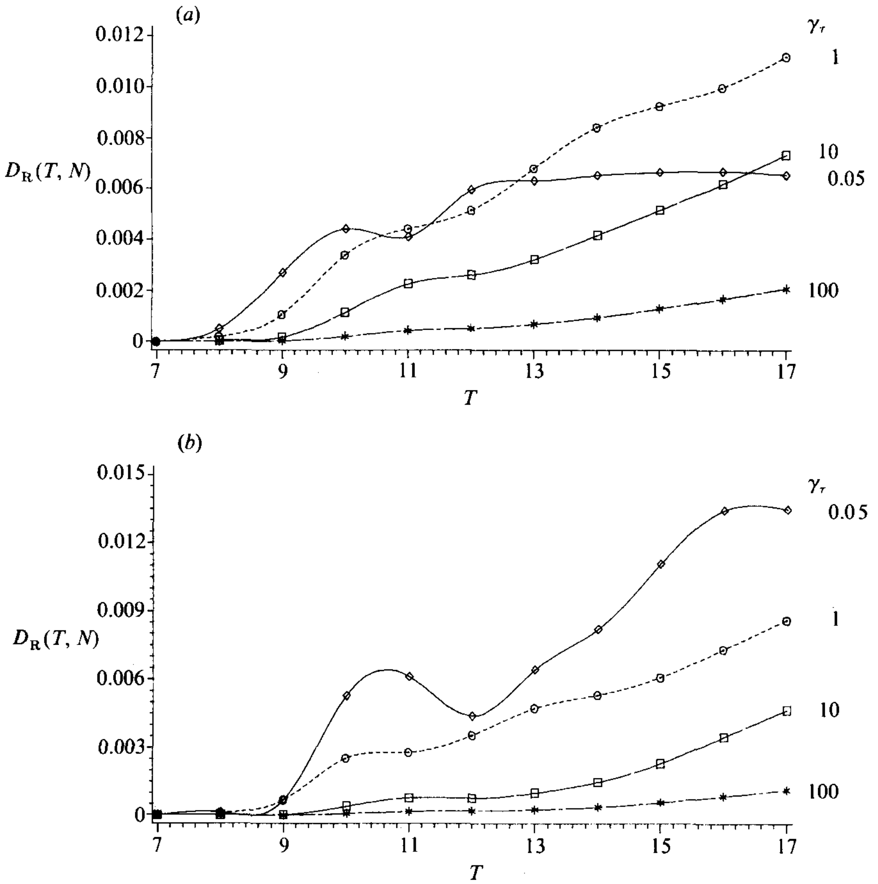

FIGURE 8. Variation of $D_R(T,N)$ as a function of dimensionless time for an established jet, (*a*) particles released between $R = 0.41$ and $R = 0.49$; (*b*) particles released between $R = 0.21$ and $R = 0.29$.

experiment, particles are distributed uniformly across the cross-section at the pipe exit, which may be more closely simulated by the particles issued in the middle region in the numerical simulation. It may be argued that particles exiting near the pipe wall will interact more with the mixing layer while the particles leaving the pipe near the centreline will be influenced basically by the core flow. Based on table 3, it is seen that the current numerical simulations predict the correct trend and the maximum deviation is 17%.

Another interesting feature is the variation of $D_R(T,N)$ as a function of time. In figures 8(*a*) and 8(*b*), $D_R(T,N)$ *vs*. $T$ for an established jet is plotted for various $\gamma_\tau$ and two different particle starting radial locations. In general more variations are noted for smaller $\gamma_\tau$ because their dispersion is more closely influenced by the large-scale structures. As $\gamma_\tau$ gets larger, the curves become more linear. They all seem to reach a constant slope after a certain time and the larger the $\gamma_\tau$, the quicker it reaches its steady-state slope.

It is also informative to show typical radial particle flux distributions at a downstream location, i.e. $x/D = 3$. At this downstream counting station, a vertical array of windows is set up with each window occupying a radial distance of $\Delta r/D = 0.1$. Figure 9(*a–f*) shows the total number of particles that have passed through the

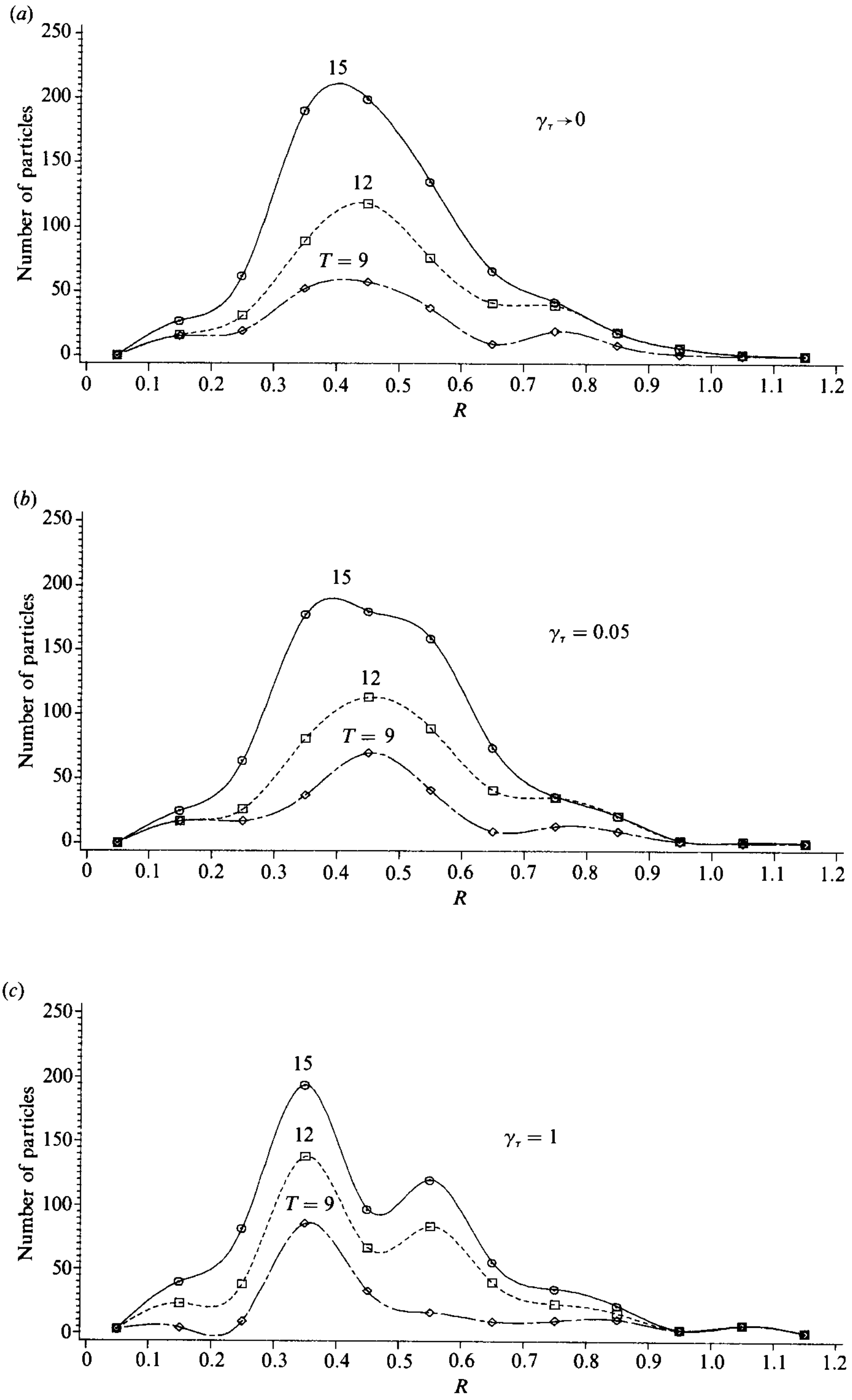

FIGURE 9(*a–c*). For caption see facing page.

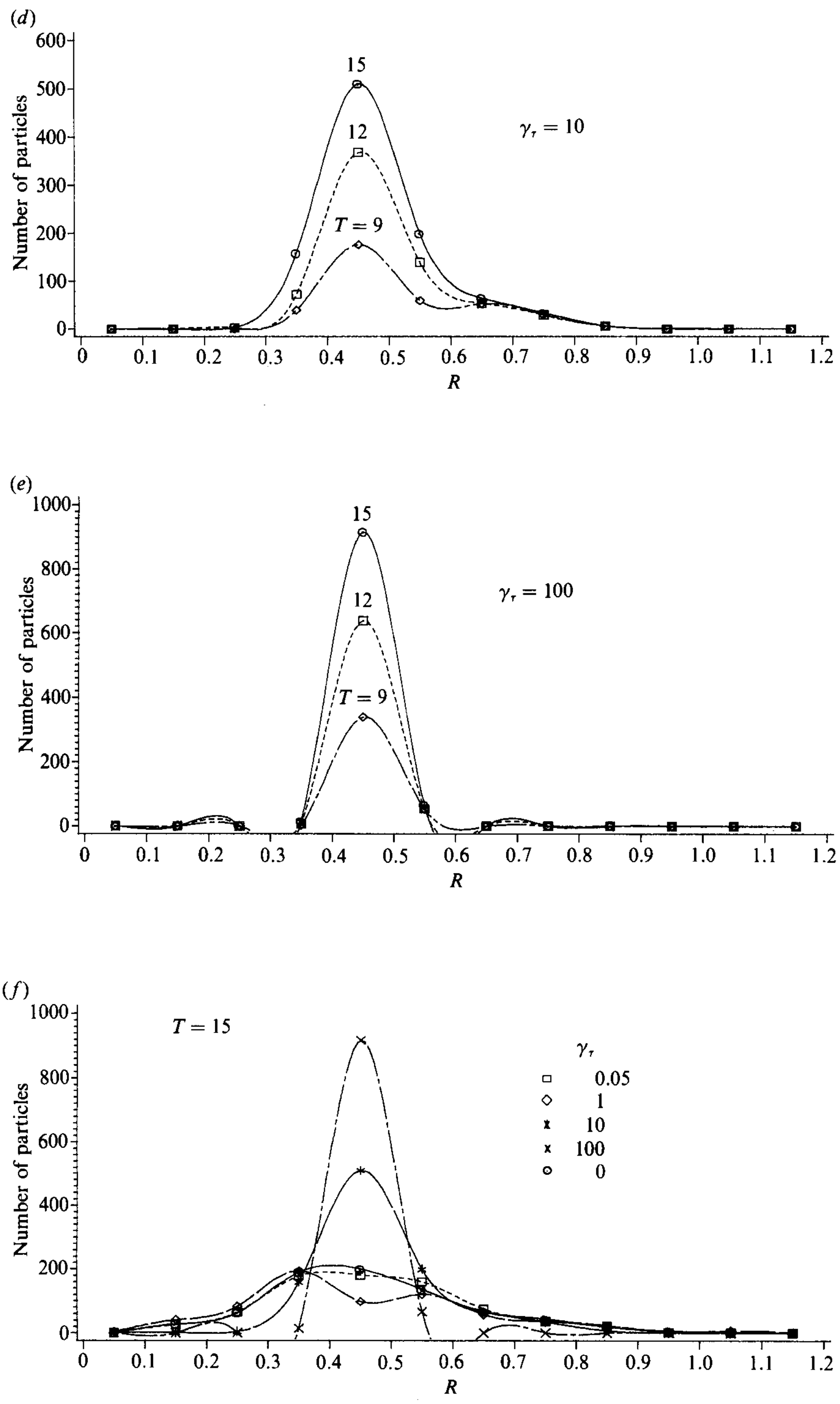

FIGURE 9. Accumulated particle radial flux distribution at $T = 9$, 12 and 15, (*a*) $\gamma_\tau \rightarrow 0$; (*b*) $\gamma_\tau = 0.05$; (*c*) $\gamma_\tau = 1$; (*d*) $\gamma_\tau = 10$; (*e*) $\gamma_\tau = 100$; (*f*) all $\gamma_\tau$ at $T = 15$.

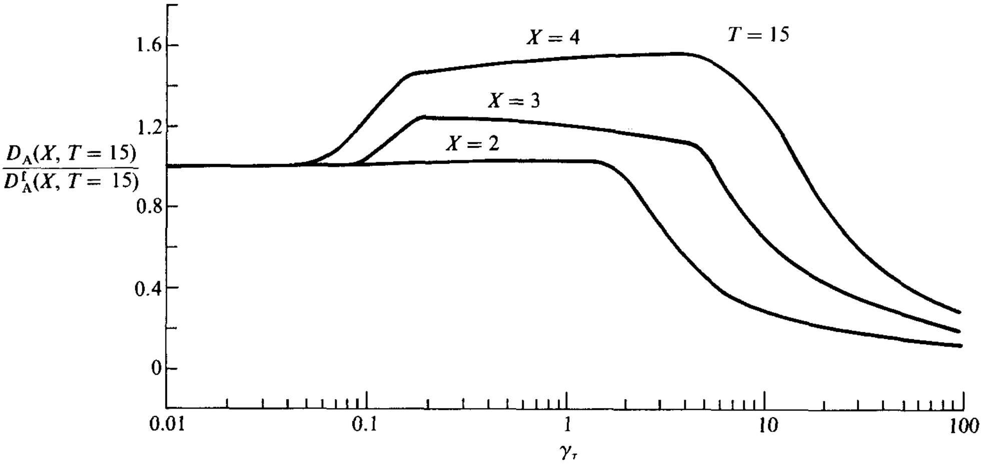

FIGURE 10. $D_A(X,T = 15)/D_A^f(X,T = 15)$ as a function of $\gamma_\tau$ for $X = 2$, 3 and 4 at $T = 15$.

windows up to a specific time as indicated in the figure. In other words each symbol represents the accumulated number of particles that have moved through this window between $T = 2$ and $T = 9$, 12 or 15. The lines connecting the symbols are formed based on the spline second-order curve-fitting technique. In figure 9(*a–f*), all the particles are introduced to the flow at the pipe exit ($x/D = 0$) and at five radial locations of 0.41, 0.43, 0.55, 0.47 and 0.49. The injection of particles starts at $T = 2$ and continues at a constant rate of a total of 1000 $U_0/D^2$ particles per metre of radial distance per second in five streams. It is noted that the accumulated radial particle flux plots show the effect of a starting jet for small times. As time becomes large, the curves become more representative of an established jet.

Figure 9(*a*) shows the accumulated particle distribution curves for tagged fluid particles in order to examine the fluid dispersion. The curves are all Gaussian-like with peaks aligned with the centre of the source and a slight asymmetry towards the outside of the jet. For $\gamma_\tau = 0.05$ the basic slope of the distribution curve is similar to that of the fluid but they are flatter. Double peaks are found for $\gamma_\tau = 1$. This is mainly due to the condition that particles are flung out of the centres of those large-scale vortices. It also explains why the two peaks are separated radially from the source. For all other cases, the single peak is well aligned with the source. For $\gamma_\tau = 10$ and 100, all the curves are Gaussian with peaks corresponding to the particle source. In figure 9(*f*), all the $T = 12$ curves are plotted together for a radial dispersion comparison. The accumulated particle distribution profiles are similar in magnitude for $\gamma_\tau \geqslant O(1)$.

In order to quantify the results shown in figure 9(*a–f*), the dispersion function at an axial location is defined as,

$$D_A(X,T) = \sum_{j=1}^{J} (M(X,T,j)(R_j(X)-0.45)^2)^{\frac{1}{2}}/M_t, \tag{28}$$

$$M_t = \sum_{j=1}^{J} M(X,T,j), \tag{29}$$

where $M(X,T,j)$ is the total number of particles that go through window $j$ between $T = 2$ and $T$ at axial location $X$. $R_j(X)$ is the radial location of the centre of window $j$ at $X$. $J$ is the total number of windows at $X$.

In figure 10, $D_{\mathrm{A}}(X, T=15)/D^{\mathrm{f}}_{\mathrm{A}}(X, T=15)$, where $D^{\mathrm{f}}_{\mathrm{A}}(X,T)$ is defined for tagged fluid particles, is plotted at three axial locations of $X = 2$, 3 and 4 for particles released between $T = 2$ and $T = 15$. Again, we are trying to see the relative particle dispersion at different downstream locations as compared with that of the fluid. The postulated physical concept of more particle lateral dispersion for $\gamma_{\tau} = O(1)$ is verified for different axial locations. Increased levels of particle dispersion are also present for increased downstream locations. This may be due to the fact that as particles travel downstream they gradually lose their axial momentum gained at the pipe exit such that they are more susceptible to the influence of the large-scale structures.

## 4. Conclusion

Numerical simulations of the particle dispersion by an axisymmetric free jet are presented. The jet flow is modelled through a discrete vortex method of vortex rings. Qualitatively, the discrete vortex simulations compare favourably with available experimental flow results concerning global flow patterns, vortex interactions and the pairing process. The predicted mean velocities and instantaneous velocity fluctuations are comparable with experimental quantities. The current flow predictions also agree well with previous numerical results by the same discrete vortex method.

For the particle dispersion simulations, it was found that the turbulent mixing layer is capable of dispersing particles with $\gamma_{\tau}$ of the order of unity beyond the boundary of the fluid dispersion if the particles enter the jet flow from near the pipe wall at the jet exit. For particles entering into the jet flow in the core region, higher particle dispersion than the fluid is calculated only for much smaller $\gamma_{\tau}$. The calculated ratios of particle dispersion to fluid dispersion for particles released in the core region compare favourably with limited results of experimental measurements. The global particle dispersion function, $D_{\mathrm{R}}(T,N)$ seems to vary with time linearly after some initial development. More high-amplitude variation of $D_{\mathrm{R}}(T,N)$ with time is predicted for smaller $\gamma_{\tau}$ because the dispersion of smaller particles is strongly influenced by the intermittency of the mixing layer. For accumulated radial flux distribution at a downstream location, similar dispersion trends to those of the global dispersion function exist. Using the fluid dispersion as a reference, particles in the range of small $\gamma_{\tau}$ are dispersed equally to the fluid, particles with large $\gamma_{\tau}$ are dispersed less than that of the fluid. Particles with intermediate $\gamma_{\tau}$ are dispersed more than the fluid particles. The results of this simulation indicate that there seems to exist a specific range of $\gamma_{\tau}$ at which optimal dispersion of particles in the turbulent mixing layer of an axisymmetric free jet may be achieved.

This research was initiated and partially completed when the first author was a participant of the NASA-Lewis Research Center 1985 Summer Faculty Program. The support of Mr D. Bulzan of NASA-Lewis is greatly appreciated. Free computing time from the Computing Center of Washington State University was essential in finishing this project. The authors wish to acknowledge the many helpful discussions they had with Professor C. T. Crowe.

## REFERENCES

ACTON, E. 1980 A modelling of large eddies in an axisymmetric jet. *J. Fluid Mech.* **98**, 1–31.

ASHURST, W. T. 1977 Numerical simulation of turbulent mixing layers via vortex dynamics. *Sandia Lab. Rep.* SAND 77-8613.

BRADSHAW, P., FERRISS, D. H. & JOHNSON, R. F. 1964 Turbulence in the noise-producing region of a circular jet. *J. Fluid Mech.* **19**, 591–624.

BROWAND, F. K. & HO, C. M. 1983 The mixing layer: an example of quasi two-dimensional turbulence. In *Two-Dimensional Turbulence: J. Mec. Theor. Appl. Special Suppl.* pp. 99–120.

CANTWELL, B. J. 1981 Organized motion in turbulent flow. *Ann. Rev. Fluid Mech.* **13**, 457–515.

CHORIN, A. J. 1973 Numerical study of slightly viscous flow. *J. Fluid Mech.* **57**, 785–796.

CLIFT, R., GRACE, J. R. & WEBER, M. E. 1978 *Bubbles, Drops, and Particles.* Academic.

CROWE, C. T. 1982 Review – Numerical models for dilute gas particle flows. *Trans. ASME* I: *J. Fluids Engng* **104**, 297–303.

CROWE, C. T., GORE, R. & TROUTT, T. R. 1985 Particle dispersion by coherent structures in free shear flows. *Particulate Science and Tech.* **3**, 149–158.

DAVIES, P. O. A. L., FISHER, M. J. & BARRATT, M. J. 1963 The characteristics of the turbulence in the mixing region of a round jet. *J. Fluid Mech.* **15**, 337–367.

GORE, R., CROWE, C. T., TROUTT, T. R. & RILEY, J. J. 1985 A numerical study of particle dispersion in large scale structures. *ASME paper* HTD – vol. 47, Multiphase Flow and Heat Transfer, BK, no. 600304.

HO, C. M. & HUERRE, P. 1984 Perturbed free shear layers. *Ann. Rev. Fluid Mech.* **16**, 365–424.

LAMB, H. 1945 *Hydrodynamics.* Dover.

LAU, J. C. & FISHER, M. J. 1975 The vortex-street structure of 'turbulent' jets. Part 1. *J. Fluid Mech.* **76**, 299–337.

LEONARD, A. 1985 Computing three-dimensional incompressible flows with vortex elements. *Ann. Rev. Fluid Mech.* **17**, 523–559.

MAXEY, M. R. & RILEY, J. J. 1983 Equation of motion for a small rigid sphere in a nonuniform flow. *Phys. Fluids* **26**, 883–889.

STUART, J. T. 1967 On finite amplitude oscillations in laminar mixing layers. *J. Fluid Mech.* **3**, 347–370.

YULE, A. J. 1978 Large-scale structure in the mixing layer of a round jet. *J. Fluid Mech.* **89**, 413–432.

YULE, A. J. 1980 Investigations of eddy coherence in jet flows. In *The Role of Coherent Structures in Modeling Turbulence and Mixing* (ed. J. Jinenez), pp. 188–207. Springer.

YUU, S., YASUKOUCHI, N., HIROSAWA, Y. & JOTAKI, T. 1978 Particle turbulent diffusion in a dust laden round jet. *AIChE J.* **24**, 509–519.